




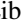


Graphene quantum dot states near defects

C. Schattauer ¹, L. Linhart ¹, T. Fabian ¹, T. Jawecki ², W. Auzinger ² and F. Libisch ^{1,*}

¹*Institute for Theoretical Physics, TU Wien, 1040 Vienna, Austria, European Union*

²*Institute of Analysis and Scientific Computing, TU Wien, 1040 Vienna, Austria, European Union*



(Received 23 July 2020; accepted 7 October 2020; published 28 October 2020)

Smoothly confined graphene quantum dots (GQDs) localize Dirac electrons with conserved spin and valley degrees of freedom. Recent experimental realization of such structures using a combination of magnetic fields and a scanning tunneling microscope tip showcased their potential in locally probing and adjusting the valley degree of freedom. The present work models the influence of lattice defects on the level structure of GQDs. We study both the adiabatic level spacing “landscape”—orbital splitting and valley splitting—as well as transition dynamics between GQD states. The system is modeled using a tight-binding approach with on-site and hopping parameters in the vicinity of the defect region extracted from density functional theory via Wannier orbitals while time propagation is done using Magnus operators. Different defect types, such as double vacancy, Stone-Wales, flower, and Si substitution, are considered. We predict tunable valley splittings of the order of 2–20 meV. The level structure can thus be tailored at will by engineering appropriate defect geometries.

DOI: [10.1103/PhysRevB.102.155430](https://doi.org/10.1103/PhysRevB.102.155430)

I. INTRODUCTION

Unique electronic properties and long spin coherence times make graphene [1–3] a promising host material for quantum dots which might one day replace GaAs as the state-of-the-art material for both spintronic [4–7] and valleytronic applications [8–10]. Unfortunately, patterning graphene to form quantum dots yields devices dominated by edge effects [11,12]. The gapless spectrum of graphene makes electrostatic confinement challenging. Recent developments towards so called edge-free quantum dots in single-layer graphene by a combination of electric and magnetic fields [13–19] pave the way for graphene quantum dots (GQDs) with a level spectrum free of edge effects.

GQDs are appealing host materials for spin qubits [5,7]. These are unfeasible without controlled breaking of the valley degree of freedom of graphene. The hexagonal symmetry of the honeycomb lattice results in two inequivalent electronic states in graphene, so-called valleys, which we label with “+” and “−.” Quantum states in pristine graphene carry this valley index $\tau = \pm$ as an additional quantum number.

In the present manuscript, we simulate the spectrum of electrostatically defined GQDs in the presence of lattice defects. In particular, we focus on the controlled breaking of the valley symmetry by defects close to the GQD. Tremendous improvement in the synthesis of graphene nanostructures [20,21] has enabled very clean samples with high mobility and low defect density. Instead of many randomly distributed defects hampering device performance, one can envision exploiting specific lattice defects in graphene which actively tune the level spectrum of edgeless GQDs in their close vicinity. The possibility to purposefully create a certain defect

density via high-energy particle beam bombardment [22–24] in graphene may ultimately develop towards systematically placing certain defects in a controlled manner.

One setup to induce smooth electrostatic confinement in single layer graphene involves combining an out-of-plane magnetic field (to ensure Landau quantization) with an electric field. The Landau level energies $E_L^{(n)}$ for pristine graphene in a perpendicular magnetic field B are given by [2]

$$E_L^{(n)} = v_F \cdot \text{sgn}(n) \sqrt{\frac{2\hbar e}{c} |B| |n|} \quad \text{with } n \in \mathbb{Z}, \quad (1)$$

with Fermi velocity v_F . The energy gaps between Landau levels ($\Delta E_0 = E_L^{(1)} - E_L^{(0)} \approx 80$ meV for $B = 7$ T) allow electrostatic confinement given a suitable electrostatic potential. This potential can be induced by a scanning tunneling microscopy (STM) tip hovering over the graphene flake [13,14] (see Fig. 1). We assume that substrate effects are small compared to the tip-induced confinement, as readily achieved using an atomically flat substrate such as hexagonal boron nitride (hBN). The STM tip locally shifts the energy relative to the Landau levels. The resulting smooth confinement avoids any physical edges and hosts fourfold near-degenerate spin-valley quadruplets [13]. The energy spacing between the quadruplets is determined by the electrostatic environment created by the STM tip. In practice [13], one finds values of the order of 10 meV, about one order of magnitude smaller than ΔE_0 . The homogeneous magnetic field used for inducing Landau quantization leads to a small spin splitting on the order of 800 μ eV (at $B = 7$ T) between the two spin doublets of the quadruplet. The GQDs defined by a mobile STM tip can easily be moved with respect to the graphene lattice, as opposed to GQDs created by patterning of the lattice. Creating the GQD with an STM tip also provides an elegant way to measure the energies of individual quantum dot states via charging events

*Corresponding author: florian.libisch@tuwien.ac.at

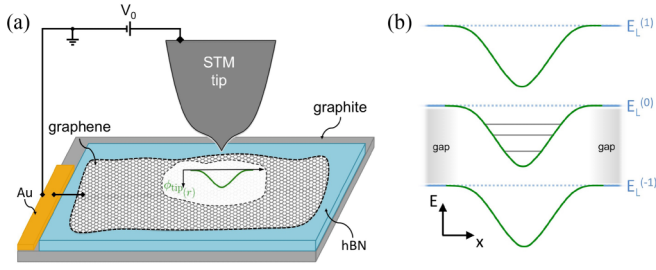


FIG. 1. (a) Schematic setup of STM tip and graphene flake on an hBN substrate. (b) Achieving confinement within the first Landau gap.

[13]. Since the spectrum of the quantum dot reacts sensitively to the local electronic environment it can be used as a sensitive probe of the local electronic structure [14]. Exchanging the STM tip for an array of electric gates could also provide motion on relevant time scales for dynamic switching between dot states.

This paper is organized as follows: We first outline our approach for accurately modeling quantum dot states in the presence of defects, and compare different levels of approximation. We then calculate the effect of several lattice defects (double vacancy, Si substitution, and flower defect) on the quantum dot states, with a particular focus on valley symmetry breaking induced by the defects. We identify several avoided crossings within the valley subspace, suggesting that the valley splitting changes sign when the dot passes through the defect. We finally show how such crossings can be exploited to dynamically obtain a desired state by transitioning the crossing either adiabatically or diabatically.

II. MODEL

We model a finite-sized, rectangular graphene flake with an area of approximately $120 \times 100 \text{ nm}^2$ using a tight-binding Hamiltonian

$$\hat{H}(E) = \sum_i s_i \hat{c}_i^\dagger \hat{c}_i + \sum_{\langle i,j \rangle} t_{ij} \hat{c}_i^\dagger \hat{c}_j + \Sigma(E), \quad (2)$$

with \hat{c}_i^\dagger (\hat{c}_i) representing the creation (annihilation) operators of a quasiparticle at site i with position r_i , s_i the on-site (diagonal) matrix elements, and t_{ij} the hopping amplitudes between sites i and j . The sum over j runs over the nearest-neighbor sites included: We use up to 10th nearest-neighbor hopping with values taken from density functional theory by Wannierization [25]. An energy-dependent self-energy [26,27] $\Sigma(E)$ implements open boundary conditions on all four sides [Fig. 2(a)]. This avoids edge effects and also filters out delocalized states [11]. We do not include physical spin. A perpendicular, homogeneous magnetic field (7 T) enters the hopping matrix elements t_{ij} via a Peierl's phase. For now, we neglect the influence of the hBN substrate, except for its effect on the electrostatic environment. We will explicitly consider the influence of (substrate-induced) disorder below. To model the electrostatic environment due to an STM tip at a voltage V_0 , we numerically solve a classical Poisson equation [13] with the following parameters: $r_{\text{tip}} = 120 \text{ nm}$, $\epsilon_{\text{hBN}} = 4$, $\epsilon_{\text{gr}} = 2.5$, and a thickness of the hBN substrate $d_{\text{hBN}} \approx 30 \text{ nm}$.

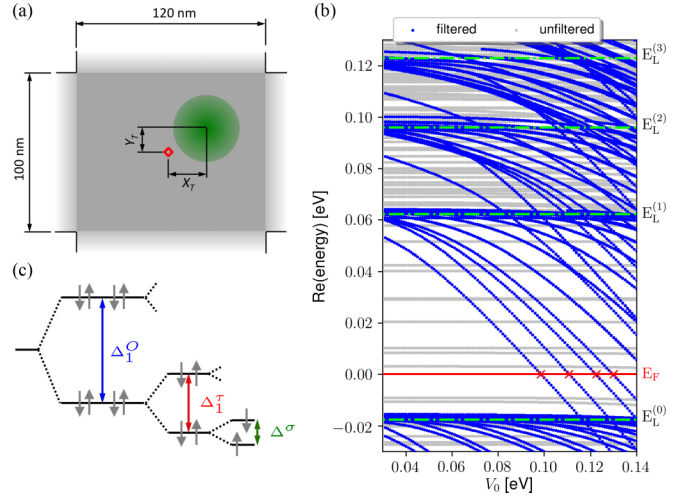


FIG. 2. (a) Schematic depiction of the model graphene flake with red marker indicating the embedding position for defects (flake center) and the green circle representing the GQD (possibly shifted relative to the defect by $\mathbf{R}_T = (X_T, Y_T)$). (b) Sequence of eigenenergies (real part) around the Dirac point for different values of tip voltage (and thus “depth” of the GQD potential) filtered for localized (low imaginary parts $\Gamma_{i,\tau}$, blue dots) and delocalized states (high imaginary parts $\Gamma_{i,\tau}$, gray dots). Landau level energies (horizontal dot-dashed green lines) as well as the Fermi level for defining occupied GQD states are indicated (red line). (c) Energy level diagram for the lowest two orbitals of a GQD with orbital splitting Δ_1^O , valley splitting Δ_1^V , and spin splitting Δ^σ indicated.

Following Ref. [28] we fit an analytic function to arrive at a rotationally symmetric potential

$$\phi_{\text{tip}}(\mathbf{r}) = \begin{cases} -V_0 \cdot \cos^5\left(\frac{\pi}{2\alpha}|\mathbf{r}|\right), & |\mathbf{r}| < \alpha, \\ 0, & |\mathbf{r}| \geq \alpha, \end{cases} \quad (3)$$

with

$$\alpha = 2309|V_0| \sqrt{1 + \sqrt{\frac{0.4}{0.005 + |V_0|}}}, \quad (4)$$

which can be easily implemented into our tight binding calculations (see Supplemental Material of [13] for details regarding the tip potential calculation). At typical tip voltages we obtain a potential well of approximately 20 nm in diameter. We then solve the eigenproblem

$$\left[\hat{H}(E_F) + \sum_l \phi_{\text{tip}}(\mathbf{r}_l - \mathbf{R}_T) \hat{c}_l^\dagger \hat{c}_l \right] |\Psi_j^\tau\rangle = \varepsilon_{j,\tau} |\Psi_j^\tau\rangle \quad (5)$$

for eigenvalues within an energy range of interest via Krylov methods [29], where j counts the orbital energy levels and $\tau = +, -$ refers to the valley index of graphene. Here, E_F is the Fermi level of the surrounding graphene, which is tuned into the bulk Landau gap to optimize confinement. We model level spacings obtained in experiment, where one scans the tip potential and detects charging events whenever a GQD level is occupied [13]. We can solve Eq. (5) for a given V_0 to determine eigenenergies $\varepsilon_{j,\tau}(V_0)$ [Fig. 2(b)]. Since the self-energy contained within the Hamiltonian breaks time-reversal

symmetry (it includes only outgoing lead modes, not incoming ones), Eq. (5) yields complex eigenvalues $\varepsilon_{j,\tau} = \varepsilon_{j,\tau} - i\Gamma_{j,\tau}$. The imaginary part $\Gamma_{j,\tau}$ describes the coupling to the environment—we can thus easily distinguish between states localized within the GQD [blue lines in Fig. 2(b)] and delocalized Bloch states [gray lines in Fig. 2(b)] ($\Gamma < 190 \mu\text{eV}$ gives a reasonable threshold). We extract the values of V_0 at which eigenvalues corresponding to localized states cross the Fermi level E_F [red crosses in Fig. 2(b)]. Recalculating for different displacements $\mathbf{R}_T = (X_T, Y_T)$ of the tip potential allows us to map out a “level spacing landscape,”

$$V_0^{j,\tau}(\mathbf{R}_T, E_F), \quad \varepsilon_{j,\tau}(\mathbf{R}_T; V_0^{j,\tau}) = E_F. \quad (6)$$

We simplify the eigenvalue problem [Eq. (5)] by evaluating the now energy-dependent Hamiltonian (due to the energy-dependent self-energy for the open boundaries) at E_F instead of $\varepsilon_{j,\tau}$ to avoid solving an otherwise quite cumbersome nonlinear eigenvalue problem. This approximation becomes exact in the limit $\varepsilon_{j,\tau} \rightarrow E_F$, which is exactly the eigenenergy of each dot-state solution in Eq. (6) [red crosses in Fig. 2(b)].

For a pristine graphene lattice, level (j, τ) crosses the Fermi level at constant tip potential [$V_0(\mathbf{R}_T) = V_0^{j,\tau} \pm 1 \mu\text{eV}$] independent of tip displacement. We conclude that there are no sizable finite-size or edge effects due to the boundary of our simulation cell.

Analytical solutions for free Dirac fermions in a magnetic field are the valley pairs [2]

$$|\psi_j^+\rangle = \begin{pmatrix} |\phi_{|j|-1}\rangle \\ |\phi_{|j|}\rangle \end{pmatrix}, \quad |\psi_j^-\rangle = \begin{pmatrix} |\phi_{|j|}\rangle \\ |\phi_{|j|-1}\rangle \end{pmatrix}, \quad (7)$$

where the $|\phi_j\rangle$ are eigenstates of a harmonic oscillator that can be expressed in Hermite polynomials. The orbital index j differs by one on the two sublattice components and, when $j \equiv 0$, the other component “ $|j| - 1$ ” vanishes.

In the case of an additional confinement potential which (approximately) conserves valley symmetry, the structure of the solution for the two valleys suggested by Eq. (7) remains intact,

$$|\psi_j^+\rangle = \begin{pmatrix} |\varphi_a\rangle \\ |\varphi_b\rangle \end{pmatrix}, \quad |\psi_j^-\rangle = \begin{pmatrix} |\varphi_b\rangle \\ |\varphi_a\rangle \end{pmatrix}, \quad (8)$$

with the $\varphi_{a,b}$ now determined numerically by the exact shape of the confinement potential. The radially symmetric tip potential in Eq. (5) suggests a description via radial ($n_r \in \mathbb{N}_0$) and angular ($m \in \mathbb{Z}$) quantum numbers for the modified GQD states. A possible adiabatic mapping from LL index N to allowed combinations of n_r and m can be formulated [30,31]. The simulated eigenstates (Fig. 3), indeed, resemble the structure suggested by the analytical solution in Eq. (7) perfectly. We obtain doubly valley degenerate GQD states ($\Delta^\tau \approx 0 \text{ meV}$), separated by orbital splittings $\Delta^O \approx 20 \text{ meV}$. Additionally considering physical spin would yield a spin splitting $\Delta^\sigma = 800 \mu\text{eV}$ at 7 T. Clean numerical separation of the degenerate valley pairs can only be achieved via a small mass term [$V_{AB} = (+1, -1) \text{ meV}$] with opposite sign on the two sublattices. In subsequent calculations that include lattice defects we use these states as reference valley states. We project the dot wave functions on the corresponding $\langle \psi_i^+ |$

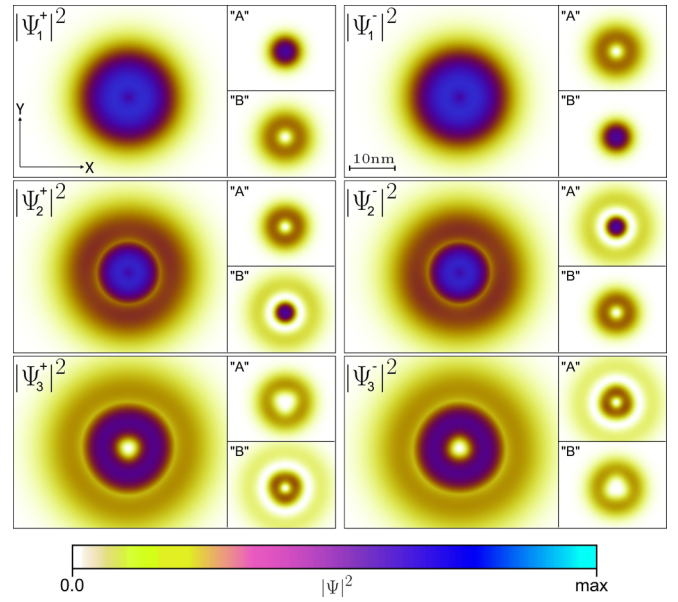


FIG. 3. Probability density of the first six (one valley pair per row) GQD eigenstates as well as their sublattice projected density (A/B insets) for the pristine system.

as a measure for the residual valley polarization

$$P_\tau = |\langle \psi_i^+ | \Psi_i^\tau \rangle|^2, \quad (9)$$

where $|\Psi\rangle$ represents a GQD state in the presence of a defect, while $|\psi\rangle$ is the corresponding state of the pristine system with the same displacement of the tip.

How do lattice defects modify the level spectrum of the GQD? We include defects at the center of our flake by suitably tuning the on-site and hopping elements in Eq. (2). Then, we study the change of the level spectrum, Eq. (5), as a function of quantum dot displacement \mathbf{R}_T [see Fig. 2(a)].

Since the quantum dot eigenstates sensitively probe the local electronic environment, care must be taken to correctly model the various defects. We consider, in order of increasing accuracy and numerical cost, different approaches for the simple case of a lattice double vacancy [32] as follows.

(a) The poor man’s description of a vacancy simply removes the corresponding orbitals entirely, while everything else remains unchanged.

More elaborate approaches are based on some level of density functional theory (DFT). We use the VASP software package for DFT calculations [33–36] and refer to our earlier work for technical details [25].

(b) Based solely on the relaxed defect geometry obtained from DFT (or, potentially, from a molecular dynamics simulation or STEM/STM measurements), one can parametrize the defect based on a simple Slater-Koster model [37,38].

Finally, one can extract tight-binding parameters directly from the DFT result, without the need for empirical models. We use Wannier90 [39–41] and project only on the carbon p_z orbitals, since those dominate the electronic structure around the Fermi energy, as follows.

(c) We extract the parametrization of the entire defect from a 6×6 DFT supercell calculation.

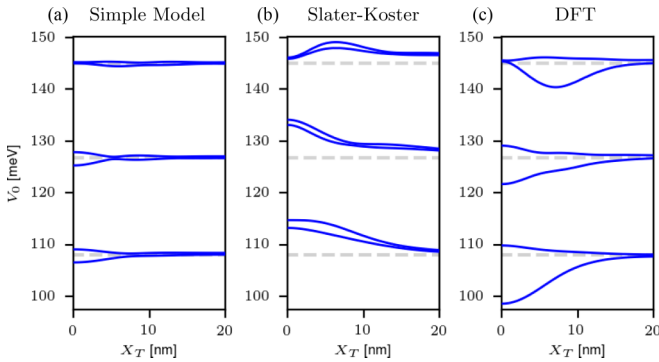


FIG. 4. Level spacing landscape for different embedding methods (see description in the “Model” section) of the double vacancy defect for GQD displacement in x direction.

In the full defect calculation (c) the tight-binding parameters obtained by Wannier90 reproduce the DFT band structures of the fully relaxed defect geometry, with a maximal deviation of 4 meV in an energy range around the Dirac point (± 1.25 eV). While numerically quite costly, this approach should be the most accurate one, and can be used to benchmark the two more approximative methods. Unfortunately, both (a) and (b) heavily underestimate the induced valley splittings compared to the fully Wannierized embedding (Fig. 4). Since the qualitative agreement of method (b) [Slater-Koster, Fig. 4(b)] also seems lacking, we conclude that using such a general parametrization is not accurate enough for the present problem (agreeing results for other defects not shown). In contrast, the very simple method (a), inherently only usable for vacancies, provides an—admittedly rough—qualitative estimate of induced valley splittings.

The asymmetry of the induced valley splitting (relative to the gray lines in Fig. 4 representing the pristine system) at displacement $X_T = 0$ is only seen when using a full DFT supercell calculation. The resulting level spectrum landscape of a defect would therefore appear to be an intricate function of all hopping terms. None of the low level methods provide a reasonable alternative to a full Wannierization of the defect supercell [method (c)]. We therefore employ method (c) in all subsequent calculations.

III. TUNABLE VALLEY SPLITTING

We investigate the influence of various defects, such as double vacancy, a silicon substitution, and a flower defect on the potential landscape $V_0^{i,\tau}(\mathbf{R}_T)$. These defects induce a sizable valley splitting Δ^τ as well as a series of avoided crossings in the valley subspace. Our findings prove robust even in the presence of moderate, long-range correlated disorder (representing influence of the hBN substrate), as outlined below. These findings suggest that a suitable arrangement of defects on the lattice can be used to engineer a desired series of avoided crossings. A graphene flake with correctly placed defects could thus serve as a scaffold for quantum-mechanical few-level systems with tailored interactions.

a. Double vacancy. A double vacancy strongly perturbs the valley symmetry of a GQD (see Fig. 5) resulting in a sizable, asymmetric valley splitting of the lowest orbital

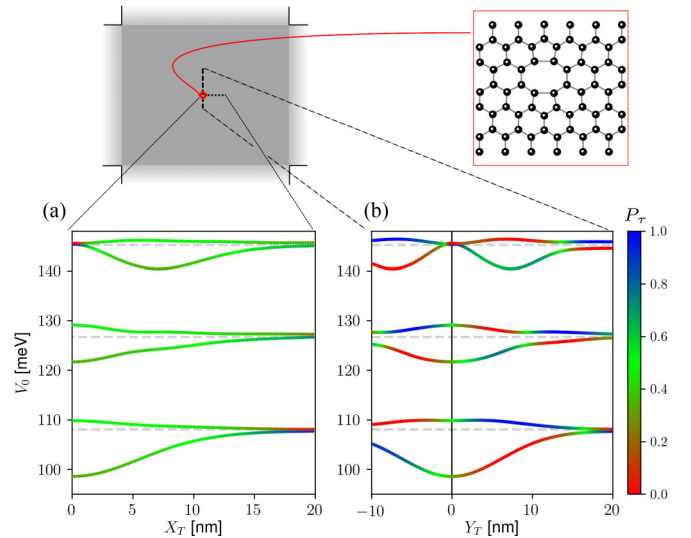


FIG. 5. Displacement dependent level spectrum for the lowest GQD states (first three valley pairs) in the presence of a double vacancy defect at the indicated position (red marker in flake schematic) for GQD displacement in (a) x direction and (b) y direction. The color scale represents the squared overlap between defect and pristine wave functions P_τ as defined in Eq. (9).

($\Delta_1^\tau \approx 13$ meV) when the tip is located at the defect, $\mathbf{R}_T = (0, 0)$. This splitting decreases for the second orbital to about 8 meV and vanishes completely for the third orbital due to the decreasing probability density of the wave functions at the GQD center (see Fig. 3). At $\mathbf{R}_T = (0, 0)$ the valley pairs split into an energetically favorable, localized state, and a delocalized state at an energy similar to the pristine system. In a double vacancy, with the sublattice corresponding to the “upper” missing atom labeled as “A,” the wave function in the upper semicircle predominantly localizes on the “B” sublattice, and vice versa for the lower hemisphere (see Fig. 6). The energy of the state is thus lowered by avoiding the intersublattice hopping to the missing atom.

The dependence of the induced valley splitting Δ_i^τ on the distance to the defect correlates with the radial density distribution of the corresponding pristine wave functions $|\psi_i^\tau\rangle$: We plot P_τ [see Eq. (9)] as color scale in the level-spacing landscapes. States with $P_\tau = 0$ (red) or 1 (blue) have perfect overlap with the pristine valley solutions of Eq. (8), whereas $P_\tau = 0.5$ (green) indicates a balanced superposition within the pristine valley basis (“valley mixing”). The splitting Δ^τ and valley mixing gradually decrease and are lost when there is no more density at the defect site. The lowest—and thus narrowest—orbitals regain the characteristic structure of Eq. (8) at a distance of about 20 nm (see red/blue color scaling associated with $P_\tau = 0, 1$ in Fig. 5).

While the magnitude of the induced valley splitting Δ^τ is independent of the direction of displacement of the GQD, the respective states differ substantially [compare Figs. 5(a) and 5(b)]. For displacements perpendicular to the axis through the two removed carbon atoms of the double vacancy (x direction in our coordinate system) we find no well-defined valley polarization P_τ , [Eq. (9), green lines in Fig. 5(a)] indicating a maximal mixing of the valley states as soon as the defect is

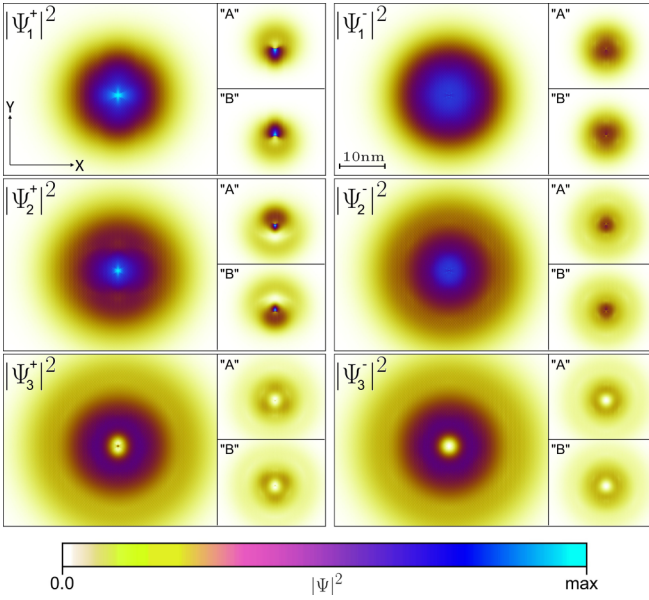


FIG. 6. Probability density in the presence of a double vacancy for $\mathbf{R}_T = (0, 0)$. The panels show the first six (one valley pair per row) GQD eigenstates as well as their sublattice projected density (A/B insets).

within the typical radius of the respective GQD orbital. At very small distances ($X_T < 5$ nm) this mixing is no longer restricted to a specific valley subspace as $P_+ + P_-$ no longer adds up to one. Displacing the GQD parallel to the double vacancy (y direction) reveals a fundamentally different evolution of P_τ including several avoided crossings connected by regions where $P_\tau \approx 0$ or 1 [Fig. 5(b)]. Displacing the tip in y direction induces an asymmetry with respect to the vacant atom positions, which leads to a sequence of avoided crossings as the maxima of probability density pass over the defect position. This asymmetry is also reflected in the sublattice projected densities [Fig. 6(top left)] and gives an intuitive understanding of the valley inversion that occurs when the tip is displaced in $\pm y$ direction.

b. Flower defect. The flower defect, a 30° rotation of a region containing seven carbon rings [42,43] [see inset in Fig. 7(a)], induces valley splittings of similar magnitude as the double vacancy at $\mathbf{R}_T = (0, 0)$ [Fig. 7(a)]. However, the split-

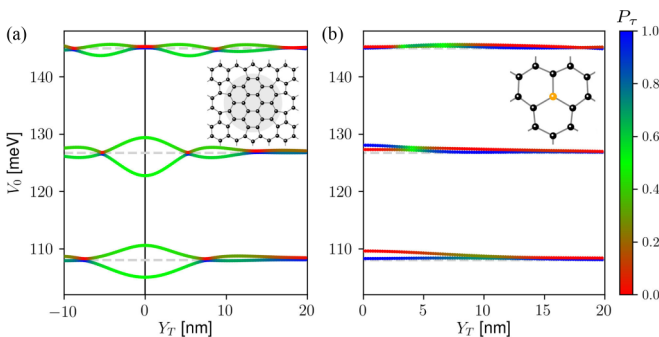


FIG. 7. GQD energies as a function of quantum dot position $\mathbf{R}_T = (X_T, Y_T)$ relative to (a) a flower defect and (b) a Si substitution defect for GQD displacement in y direction.

ting opens in a very symmetric way, $\varepsilon_{\pm}^{\text{flower}} \approx \varepsilon_0 \pm \Delta^\tau/2$ [gray dashed lines in Fig. 7(a)], while the strong localization at the double vacancy site induces an asymmetric valley splitting, $\varepsilon_+^{\text{vacancy}} \approx \varepsilon_0$ and $\varepsilon_-^{\text{vacancy}} \approx \varepsilon_0 - \Delta^\tau$. Despite being a pure relocation defect with comparatively large extent, the level spectrum seems to approach the pristine limit much sooner when increasing the GQD-defect distance. Moving the GQD in x direction produces an almost identical response of the levels as in Fig. 7(a), confirming the well preserved rotational symmetry of the flower defect.

c. Silicon substitution. The level spectrum with a silicon substitution defect [44] shows far smaller valley splittings (2 meV for the lowest orbital). Its comparatively weak perturbation to the valley symmetry is also reflected by values of P_τ close to 0 and 1 (red/blue color scale) with very narrow avoided crossings. The lowest orbital shows no valley inversion at all [Fig. 7(b)].

d. Magnetic field. The magnetic field is what enables smooth confinement in the first place by creating the confinement gap due to Landau quantization. We want to emphasize that increasing (decreasing) the magnitude of the magnetic field to first order only resizes this confinement gap and thus merely globally shifts the level spectrum landscape to higher (lower) values of V_0 . Investigating the system at different field strengths (not shown) reveals that valley splittings Δ_i^τ are not significantly sensitive to the magnetic field strength.

e. Disorder. Some additional disorder (e.g., due to substrate interaction) will undoubtedly be present in the experiment. We create a correlated disorder potential $V_D(\mathbf{r})$ with various correlation lengths l_{corr} and amplitudes $V_D^0 = \sqrt{\langle V_D^2 \rangle}$, and $\langle V_D \rangle = 0$, by convolution of uncorrelated disorder with a Gaussian kernel. This should adequately represent the typical potential landscape of graphene on a nonaligned hBN substrate even in the presence of possible defects/impurities in the hBN.

Very large l_{corr} of the order of the GQD size (FWHM ≈ 20 nm) merely result in global shifts to all GQD levels with almost no changes to the level splittings. In contrast, the influence of short-ranged disorder is *a priori* not clear. However, since our system is deep in the Landau regime, another important length scale is given by the magnetic length ($l_B \propto 1/\sqrt{B}$), which in our case ($|\vec{B}| \approx 7$ T) evaluates to about 9.4 nm. The system thus averages over disorder on length scales below this limit, and since $\langle V_D \rangle = 0$ the level spectrum landscape recovers the unperturbed shape.

We consider valley projections for the double vacancy (Fig. 8) as in (Fig. 6), but with additional disorder. Both the induced valley splitting as well as the wave function character P_τ are robust for various amplitudes and characteristic length scales of the disorder. Typical disorder up to a strength of 10 meV with correlation lengths between 1.5 nm and 15 nm only slightly distorts the level spectrum landscape and, most importantly, has no effect on the magnitude of the level splitting. The two main changes of the wave function due to disorder are (i) some density is induced at the vacancy site [$|\Psi_i^\tau|^2(\mathbf{r} = 0) \neq 0$] for all orbitals, which leads to valley mixing, and (ii) regions of low values of P_τ for large V_D (green color scale in Fig. 8) appear because the valley doublet in the pristine basis becomes poorly suited to accurately represent the distorted wave functions.

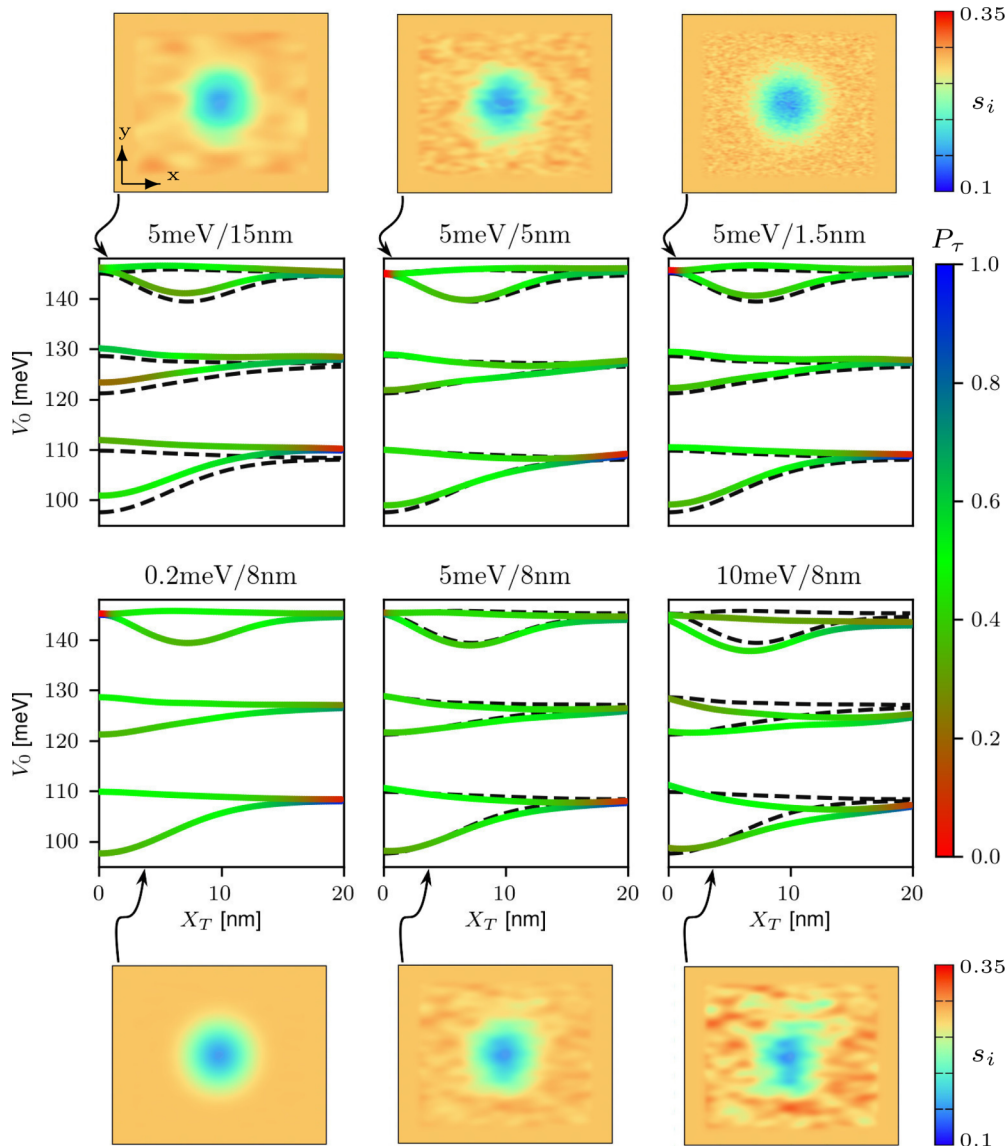


FIG. 8. Level spectrum landscapes for the double vacancy defect (with GQD displacement in x direction) in the presence of correlated disorder (dashed black lines correspond to vanishing disorder). The subplots are labeled with values for both $\sqrt{\langle V_D^2 \rangle}$ and l_{corr} . Each subplot is additionally referenced by a sketch of the total on-site potential s_i (eV) throughout the graphene flake ($120 \times 100 \text{ nm}^2$) to put the included disorder into perspective.

IV. TRANSITION DYNAMICS

In the static system, lattice defects can induce sizable valley splittings Δ^τ of an order comparable to the orbital splitting Δ^O . We now investigate the dynamics of moving the GQD with respect to the defect on time scales relevant for the electronic dynamics. We find that dynamically traversing the GQD in the vicinity of such defects provides an elegant approach to drive transition between GQD states. An experimental realization will require much shorter time scales than those accessible via moving an STM tip. While dynamically generating a moving potential well via electronic gates seems plausible, fabricating an array of gates on the nm scale (as is required for this task) remains a challenging aspect with current resolution limits of electron beam lithography [45].

To elucidate the dynamics near an avoided crossing between two valley states, we consider a toy Hamiltonian of the form

$$H(t) = \frac{1}{2} \begin{bmatrix} \alpha t & \Delta \\ \Delta & -\alpha t \end{bmatrix}, \quad (10)$$

describing the general structure of an avoided crossing: for the diabatic Hamiltonian with conserved symmetry (i.e., $\Delta = 0$), the two eigenenergies become degenerate at $t = 0$. For broken symmetry (i.e., finite Δ), degenerate perturbation theory yields an avoided crossing with an energy spacing of Δ . Landau-Zener theory [46,47] provides a straightforward analytical approach to estimate the diabatic transition probabilities for propagating an initially valley-pure eigenstate past

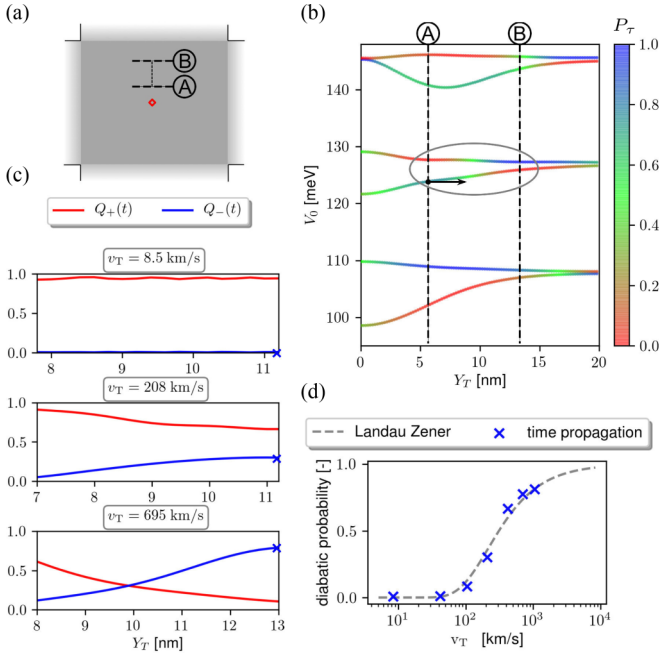


FIG. 9. (a) Schematic overview of the graphene flake with initial and final y coordinate of the GQD center indicated by lines labeled “A” and “B.” (b) Level spectrum landscape of the double vacancy defect with the avoided crossing between levels 3 and 4 centered between lines A and B which correspond to the ones in (a). (c) Squared projections (as labeled) of the propagated state as a function of y coordinate. (d) Final values of the projections in (c) superposed onto the analytical function for the diabatic transition probability.

the avoided crossing:

$$\rightarrow P_{\text{diabatic}}^{(\text{LZ})} \propto \exp\left(-\frac{\pi \Delta^2}{2\alpha}\right). \quad (11)$$

The movement of the GQD is parametrized by the time t , and thus $\alpha = v_T \cdot |\nabla_{\mathbf{r}}(\varepsilon_{i,-} - \varepsilon_{i,+})|$, where $v_T = \partial_t \mathbf{R}_T$ is the traversal velocity of the GQD. The second term represents the slope of the spectral landscape of a valley doublet in real space. Close to an avoided crossing we consider one valley doublet as an effective two level system ($\Delta^\tau \ll \Delta^0$) such as the one modeled by the toy Hamiltonian of Eq. (10). Different traversal velocities v_T allow for either adiabatic (low speeds) or diabatic (high speeds) propagation of an initial eigenstate. To simulate the dynamics, we use state-of-the-art time propagation via Magnus operators with adaptive time steps based on computable upper error bounds for the Krylov approximation [48] and error estimates of the Magnus integrator [49]:

$$|\Psi(t_B)\rangle = \hat{U}(t_B, t_A) |\Psi_2^+\rangle. \quad (12)$$

We propagate an initial state $|\Psi_2^+\rangle$ at $(X_T, Y_T) = (0, 5.6)$ nm, indicated by the black dot and arrow in [Fig. 9(b)], from A to B [see Fig. 9(a)]. The crossing has to be approached by an instantaneous GQD eigenstate in level “1” with a well defined velocity v_T . We therefore have to smoothly accelerate from a static eigenstate, which restricts the selection of possible crossings. We choose a rather wide [i.e., large

Δ in Eq. (10)] avoided crossing [between third and fourth GQD level of the double vacancy in y direction; see Fig. 9(b)]. An even wider avoided crossing would require a larger traversal velocity to achieve diabatic switching [Eq. (11)], reaching values that cannot be sufficiently smoothly accelerated to, because the neighboring avoided crossings would be in too close proximity. Narrower [i.e., small value for Δ in Eq. (10)] avoided crossings [e.g., see the avoided crossings generated by the flower defect in Fig. 7(a)] would result in much too long traversal times (this time for the adiabatic result) beyond our computational time limits. In experiment much larger time scales would be accessible and thus narrower avoided crossings should be considered.

As we propagate our initial wave function from A to B (Fig. 9) we project $|\Psi(t)\rangle$ onto the third ($|\Psi_2^+\rangle$) and fourth ($|\Psi_2^-\rangle$) orbitals of the static calculations of the otherwise identical system. The projection $Q_\tau(t)$ on the valley $\tau = \pm$ at displacement $X_T(t)$ is given by

$$Q_+(t) = |\langle \Psi_2^+ | \Psi(t) \rangle|^2, \quad Q_-(t) = |\langle \Psi_2^- | \Psi(t) \rangle|^2, \quad (13)$$

and shown in Fig. 9(c). Note that we project onto the static defect state at the same GQD position, not the pristine state.

Performing these calculations for a range of different traversal velocities v_T reveals the expected diabatic switching for faster traversal. We calculate the “final” projection values of $\langle \Psi_2^- | \Psi(t) \rangle^2$ after the avoided crossing has been traversed [blue crosses in Fig. 9(c)] as a function of the corresponding velocity [Fig. 9(d)]. We find surprisingly good agreement with the simple two-level Landau-Zener formalism. The distorted nature of the underlying avoided crossing impedes a precise evaluation of the parameters $|\nabla_{\mathbf{r}}(\varepsilon_{i,-} - \varepsilon_{i,+})|$ and Δ used in the Landau-Zener formula. Due to the exponential sensitivity of the transition curve on these parameters, a fit to our numerical data for the transition probability in Fig. 9(d) is much more accurate than estimating these parameters directly from the shape of the avoided crossing in Fig. 9(b). We thus determine $|\nabla_{\mathbf{r}}(\varepsilon_{i,-} - \varepsilon_{i,+})| = 163 \mu\text{eV}/\text{nm}$ and $\Delta = 1.9 \text{ meV}$ from a fit to the data points in [Fig. 9(d)], and find these values entirely consistent with the shape of the avoided crossing of the level spacing landscape. Quantitatively predicting the required transition speed from the shape of the avoided crossings might thus prove difficult. Nevertheless, the qualitative dependence of the diabatic transition probability on the traversal speed still offers an elegant way to enact controlled transitions between GQD levels, a necessary first step for possible applications in emerging quantum technologies.

V. CONCLUSIONS

We have modeled the response of the level spectrum of smoothly confined graphene quantum dots to lattice defects in tight-binding calculations. By embedding a local defect parametrization, obtained from Wannier-projection of DFT super cell calculations, we present an elegant way of manipulating the level spectrum of edge-free GQDs by making use of some common imperfections of graphene lattice structures. We identify several avoided crossings within the valley

doublets for the different quantum dot states. Conversely, measuring the evolution of the quantum dot eigenenergies with dot position would provide a sensitive probe for the electronic structure of the defect. Transition dynamics in these GQD-defect systems are well described by Landau-Zener theory. The predicted defect-induced valley splittings Δ^{τ} on the order of up to 12 meV should be experimentally accessible and warrant future research.

ACKNOWLEDGMENTS

We acknowledge support from the FWF DACH Project No. I3827-N36, COST Action No. CA18234, the doctoral college Solids4Fun No. W1243-N16 funded by the FWF, and the doctoral college TU-D funded by TU Wien. Numerical calculations were performed on the Vienna Scientific Clusters VSC3 and VSC4.

-
- [1] K. S. Novoselov, V. I. Falko, L. Colombo, P. R. Gellert, M. G. Schwab, and K. Kim, *Nature (London)* **490**, 192 (2012).
- [2] A. H. Castro Neto, F. Guinea, N. M. R. Peres, K. S. Novoselov, and A. K. Geim, *Rev. Mod. Phys.* **81**, 109 (2009).
- [3] D. Abergel, V. Apalkov, J. Berashevich, K. Ziegler, and T. Chakraborty, *Adv. Phys.* **59**, 261 (2010).
- [4] R. Hanson, L. P. Kouwenhoven, J. R. Petta, S. Tarucha, and L. M. K. Vandersypen, *Rev. Mod. Phys.* **79**, 1217 (2007).
- [5] B. Trauzettel, D. V. Bulaev, D. Loss, and G. Burkard, *Nat. Phys.* **3**, 192 (2007).
- [6] P. Recher, E. V. Sukhorukov, and D. Loss, *Phys. Rev. Lett.* **85**, 1962 (2000).
- [7] P. Recher and B. Trauzettel, *Nanotechnology* **21**, 302001 (2010).
- [8] J. R. Schaibley, H. Yu, G. Clark, P. Rivera, J. S. Ross, K. L. Seyler, W. Yao, and X. Xu, *Nat. Rev. Mater.* **1**, 16055 (2016).
- [9] D. Gunlycke and C. T. White, *Phys. Rev. Lett.* **106**, 136806 (2011).
- [10] G. Pacchioni, *Nat. Rev. Mater.* **5**, 480 (2020).
- [11] D. Bischoff, M. Eich, F. Libisch, T. Ihn, and K. Ensslin, *Appl. Phys. Lett.* **107**, 203107 (2015).
- [12] B. Terrés, L. A. Chizhova, F. Libisch, J. Peiro, D. Jörgner, S. Engels, A. Girschik, K. Watanabe, T. Taniguchi, S. V. Rotkin, J. Burgdörfer, and C. Stampfer, *Nat. Commun.* **7**, 11528 (2016).
- [13] N. M. Freitag, L. A. Chizhova, P. Nemes-Incze, C. R. Woods, R. V. Gorbachev, Y. Cao, A. K. Geim, K. S. Novoselov, J. Burgdörfer, F. Libisch *et al.*, *Nano Lett.* **16**, 5798 (2016).
- [14] N. M. Freitag, T. Reisch, L. A. Chizhova, P. Nemes-Incze, C. Holl, C. R. Woods, R. V. Gorbachev, Y. Cao, A. K. Geim, K. S. Novoselov *et al.*, *Nat. Nanotechnol.* **13**, 392 (2018).
- [15] D. Subramaniam, F. Libisch, Y. Li, C. Pauly, V. Geringer, R. Reiter, T. Mashoff, M. Liebmann, J. Burgdörfer, C. Busse, T. Michely, R. Mazzarello, M. Pratzer, and M. Morgenstern, *Phys. Rev. Lett.* **108**, 046801 (2012).
- [16] H.-Y. Chen, V. Apalkov, and T. Chakraborty, *Phys. Rev. Lett.* **98**, 186803 (2007).
- [17] G. Giavaras and F. Nori, *Phys. Rev. B* **85**, 165446 (2012).
- [18] G. Giavaras, P. Maksym, and M. Roy, *J. Phys.: Condens. Matter* **21**, 102201 (2008).
- [19] M. Morgenstern, N. Freitag, A. Nent, P. Nemes-Incze, and M. Liebmann, *Ann. Phys. (NY)* **529**, 1700018 (2017).
- [20] F. Bonaccorso, A. Lombardo, T. Hasan, Z. Sun, L. Colombo, and A. C. Ferrari, *Mater. Today* **15**, 564 (2012).
- [21] L. Banszerus, M. Schmitz, S. Engels, J. Dauber, M. Oellers, F. Haupt, K. Watanabe, T. Taniguchi, B. Beschoten, and C. Stampfer, *Sci. Adv.* **1**, e1500222 (2015).
- [22] W. Tian, W. Li, W. Yu, and X. Liu, *Micromachines* **8**, 163 (2017).
- [23] M. C. Lemme, D. C. Bell, J. R. Williams, L. A. Stern, B. W. H. Baugher, P. Jarillo-Herrero, and C. M. Marcus, *ACS Nano* **3**, 2674 (2009).
- [24] N. Kalhor, S. A. Boden, and H. Mizuta, *Microelectron. Eng.* **114**, 70 (2014).
- [25] L. Linhart, J. Burgdörfer, and F. Libisch, *Phys. Rev. B* **97**, 035430 (2018).
- [26] S. Sanvito, C. J. Lambert, J. H. Jefferson, and A. M. Bratkovsky, *Phys. Rev. B* **59**, 11936 (1999).
- [27] N. Papior, Computational Tools and Studies of Graphene Nanostructures, Ph.D. thesis, Technical University of Denmark, Center for Nanostructured Graphene, 2016.
- [28] P. A. Maksym, M. Roy, M. F. Craciun, S. Russo, M. Yamamoto, S. Tarucha, and H. Aoki, *J. Phys.: Conf. Ser.* **245**, 012030 (2010).
- [29] *ARPACK Users Guide* (Society for Industrial and Applied Mathematics, Philadelphia, PA, 1998), pp. 1–7.
- [30] S. Schnez, K. Ensslin, M. Sigrist, and T. Ihn, *Phys. Rev. B* **78**, 195427 (2008).
- [31] P. Recher, J. Nilsson, G. Burkard, and B. Trauzettel, *Phys. Rev. B* **79**, 085407 (2009).
- [32] We avoid the case of a single vacancy since the resulting defect state features a strong spin polarization.
- [33] G. Kresse and J. Furthmüller, *Phys. Rev. B* **54**, 11169 (1996).
- [34] G. Kresse and J. Furthmüller, *Comput. Mater. Sci.* **6**, 15 (1996).
- [35] G. Kresse and J. Hafner, *Phys. Rev. B* **47**, 558 (1993).
- [36] G. Kresse and J. Hafner, *Phys. Rev. B* **49**, 14251 (1994).
- [37] M. Koshino, *New J. Phys.* **17**, 015014 (2015).
- [38] J. C. Slater and G. F. Koster, *Phys. Rev.* **94**, 1498 (1954).
- [39] N. Marzari and D. Vanderbilt, *Phys. Rev. B* **56**, 12847 (1997).
- [40] A. A. Mostofi, J. R. Yates, G. Pizzi, Y.-S. Lee, I. Souza, D. Vanderbilt, and N. Marzari, *Comput. Phys. Commun.* **185**, 2309 (2014).
- [41] I. Souza, N. Marzari, and D. Vanderbilt, *Phys. Rev. B* **65**, 035109 (2001).
- [42] T. Björkman, S. Kurasch, O. Lehtinen, J. Kotakoski, O. V. Yazyev, A. Srivastava, V. Skakalova, J. H. Smet, U. Kaiser, and A. V. Krasheninnikov, *Sci. Rep.* **3**, 3482 (2013).
- [43] E. Cockayne, G. M. Rutter, N. P. Guisinger, J. N. Crain, P. N. First, and J. A. Stroscio, *Phys. Rev. B* **83**, 195425 (2011).

- [44] H. Inani, K. Mustonen, A. Markevich, E.-X. Ding, M. Tripathi, A. Hussain, C. Mangler, E. I. Kauppinen, T. Susi, and J. Kotakoski, *J. Phys. Chem. C* **123**, 13136 (2019).
- [45] V. R. Manfrinato, L. Zhang, D. Su, H. Duan, R. G. Hobbs, E. A. Stach, and K. K. Berggren, *Nano Lett.* **13**, 1555 (2013).
- [46] C. Wittig, *J. Phys. Chem. B* **109**, 8428 (2005).
- [47] C. Zener, *Proc. R. Soc. London, Ser. A* **137**, 696 (1932).
- [48] T. Jawecki, W. Auzinger, and O. Koch, *BIT Numer. Math.* **60**, 157 (2019).
- [49] W. Auzinger, H. Hofstätter, O. Koch, M. Quell, and M. Thalhammer, *M2AN: Math. Model. Numer. Anal.* **53**, 197 (2019).